

See discussions, stats, and author profiles for this publication at: <https://www.researchgate.net/publication/228361890>

# The Excitonic Exchange Splitting and Radiative Lifetime in PbSe Quantum Dots

ARTICLE *in* NANO LETTERS · APRIL 2007

Impact Factor: 13.59 · DOI: 10.1021/nl071219f

---

CITATIONS

89

---

READS

94

3 AUTHORS, INCLUDING:



Joonhee M. An

University of Nebraska at Lincoln

19 PUBLICATIONS 530 CITATIONS

SEE PROFILE



Alex Zunger

University of Colorado Boulder

768 PUBLICATIONS 51,027 CITATIONS

SEE PROFILE

# The Excitonic Exchange Splitting and Radiative Lifetime in PbSe Quantum Dots

J. M. An, A. Franceschetti,\* and A. Zunger

National Renewable Energy Laboratory, Golden, Colorado 80228

Received May 23, 2007

## ABSTRACT

An exciton evolving from an  $m$ -fold degenerate hole level and an  $n$ -fold degenerate electron level has a nominal  $m \times n$  degeneracy, which is often removed by electron–hole interactions. In PbSe quantum dots, the degeneracy of the lowest-energy exciton is  $m \times n = 64$  because both the valence-band maximum and the conduction-band minimum originate from the 4-fold degenerate (8-fold including spin) L valleys in the Brillouin zone of bulk PbSe. Using a many-particle configuration-interaction approach based on atomistic single-particle wave functions, we have computed the fine structure of the lowest-energy excitonic manifold of two nearly spherical PbSe quantum dots of radius  $R = 15.3$  and  $30.6$  Å. We identify two main energy splittings, both of which are accessible to experimental probe: (i) The intervalley splitting  $\delta$  is the energy difference between the two near-edge peaks of the absorption spectrum. We find  $\delta = 80$  meV for  $R = 15.3$  Å and  $\delta = 18$  meV for  $R = 30.6$  Å. (ii) The exchange splitting  $\Delta_x$  is the energy difference between the lowest-energy optically dark exciton state and the first optically bright exciton state. We find that  $\Delta_x$  ranges between 17 meV for  $R = 15.3$  Å, and 2 meV for  $R = 30.6$  Å. We also find that the room-temperature radiative lifetime is  $\tau_R \sim 100$  ns, considerably longer than the  $\sim 10$  ns radiative lifetime of CdSe dots, in quantitative agreement with experiment.

Quantum-dot excitonic states that couple hole states  $h_i$  with electron states  $e_j$  are split by electron–hole Coulomb and exchange interactions.<sup>1</sup> Recent measurements<sup>2–7</sup> and calculations<sup>6,8–11</sup> have revealed interesting physical trends in these splittings, including the emergence of short-range (scaling as  $1/R^3$  with the size of the dot) and long-range<sup>8–10</sup> (scaling as  $1/R$ ) exchange interactions. The phenomenology of the excitonic manifold depends on the electronic structure of the bulk quantum-dot material, as well as the shape and symmetry of the quantum dots. In this regard, we can identify four different types of exchange splitting patterns:

(i) Spherical dots made of a direct-gap,  $\Gamma$ -to- $\Gamma$  *zinc-blende* material (e.g., InP,<sup>7,8</sup> InAs,<sup>2</sup> and CdS<sup>3</sup>). These dots have the  $T_d$  point group symmetry, so the first hole level, corresponding to the valence-band maximum (VBM), is orbitally doubly degenerate ( $h_1 + h_2$ ), while the first electron level, corresponding to the conduction-band minimum (CBM), is orbitally nondegenerate ( $e_1$ ). Each electron and hole state is spin degenerate, so the lowest-energy excitonic manifold  $(h_1 + h_2) \otimes (e_1)$  is 8-fold degenerate at the single-particle level. Electron–hole exchange interactions split this manifold into a lower-energy “dark” quintuplet and a higher-energy “bright” triplet, separated by the exchange splitting  $\Delta_x$ , as shown schematically in Figure 1a. Deviations from the  $T_d$

Exciton splitting of different quantum dots prototypes				
$h_{3,4}e_1 \left\{ \begin{array}{l} \text{---(x3)---} \\ \text{---(x5)---} \end{array} \right.$ $h_{1,2}e_1 \left\{ \begin{array}{l} \text{---(x3)---} \\ \text{---(x5)---} \end{array} \right.$	$h_2e_1 \left\{ \begin{array}{l} \text{---(x1)---} \\ \text{---(x2)---} \\ \text{---(x1)---} \end{array} \right.$ $h_1e_1 \left\{ \begin{array}{l} \text{---(x2)---} \\ \text{---(x2)---} \end{array} \right.$	$h_{so}e_1 \left\{ \begin{array}{l} \text{---(x2)---} \\ \text{---(x1)---} \end{array} \right.$ $h_{1,2,3}e_{1,2,3} \left\{ \begin{array}{l} \text{---(x3)---} \\ \text{---(x3)---} \\ \text{---(x9)---} \\ \text{---(x9)---} \\ \text{---(x6)---} \\ \text{---(x3)---} \end{array} \right.$	$h_{so}e_1 \left\{ \begin{array}{l} \text{---(x3)---} \\ \text{---(x1)---} \end{array} \right.$ $h_{1,2}e_1 \left\{ \begin{array}{l} \text{---(x3)---} \\ \text{---(x5)---} \end{array} \right.$	$h_2e_2 \left\{ \begin{array}{l} \text{---(x3)---} \\ \text{---(x1)---} \end{array} \right.$ $h_1e_1 \left\{ \begin{array}{l} \text{---(x3)---} \\ \text{---(x1)---} \end{array} \right.$
(a) InP, CdS Zinc-blende VBM: $\Gamma$ CBM: $\Gamma$	(b) CdSe Wurtzite VBM: $\Gamma$ CBM: $\Gamma$	(c) Si Diamond VBM: $\Gamma$ CBM: X	(d) Ge Diamond VBM: $\Gamma$ CBM: L	(e) PbSe Rock-salt VBM: L CBM: L

**Figure 1.** Schematic diagram of exciton splitting of five types of quantum dots, as obtained from atomistic pseudopotential calculations (see ref 8 for InP and CdSe, ref 10 for Si, and ref 11 for Ge). In each case, we show the single-particle hole levels ( $h_1, h_2, \dots$ ) and electron levels ( $e_1, e_2, \dots$ ) that constitute the main components of an exciton. In the case of Ge,  $h_{so}$  denotes the split-off hole energy level. The degeneracy of each exciton is given as  $\times 5, \times 3$ , etc. Solid (dashed) lines indicate optically bright (dark) states. Spin–orbit interaction is neglected in (c). Excitonic levels that appear between the  $(h_1) \otimes (e_1)$  and  $(h_2) \otimes (e_2)$  manifolds in (e) are omitted for clarity.

symmetry will introduce further splittings in the dark and bright multiplets.

\* Corresponding author. E-mail: alberto\_franceschetti@nrel.gov.

(ii) Spherical dots made of a direct-gap,  $\Gamma$ -to- $\Gamma$  wurtzite material (e.g., CdSe<sup>4,6,8,9</sup>). Here the  $h_1$  and  $h_2$  single-particle levels (which are degenerate in the zinc-blende structure) are split by crystal-field effects. The  $(h_1) \otimes (e_1)$  and the  $(h_2) \otimes (e_1)$  manifolds are each 4-fold degenerate at the single-particle level. Electron–hole exchange interactions split the 4-fold  $(h_1) \otimes (e_1)$  excitonic manifold into a lower-energy, dark doublet, and a higher-energy, bright doublet, separated by the exchange splitting  $\Delta_x$ . The higher-energy  $(h_2) \otimes (e_1)$  excitonic manifold splits into a lower-energy dark state and two higher-energy bright states (Figure 1b).

(iii) Spherical dots made of an indirect-gap  $\Gamma$ -to-X diamond-like material (e.g., Si<sup>5,10</sup>). These dots have the diamond point-group symmetry  $O_h$ , so the VBM is orbitally doubly degenerate ( $h_1 + h_2$ ). Unlike case (i) above, however, the CBM states derive from the X valleys of the bulk Brillouin zone, which are spatially 3-fold degenerate. This degeneracy is split by quantum confinement effects, which lead to three nondegenerate CBM levels ( $e_1, e_2, e_3$ ) belonging to different irreducible representations. The exciton manifold, which has 24 dimensions (including spin), exhibits a complex excitonic fine structure, with dark spin-triplet states located below bright spin-singlet states, as shown in Figure 1c (spin–orbit interaction is not included in Figure 1c).

(iv) Spherical dots made of an indirect-gap,  $\Gamma$ -to-L diamond-like material (e.g., Ge<sup>11</sup>). These dots have the diamond point-group symmetry, so the VBM is orbitally doubly degenerate ( $h_1 + h_2$ ). The CBM states derive from the four L points of the bulk Brillouin zone. The degeneracy of the L points is split by quantum confinement effects, leading to four orbitally nondegenerate CBM levels ( $e_1, e_2, e_3, e_4$ ). The excitonic manifold  $(h_1 + h_2) \otimes (e_1 + e_2 + e_3 + e_4)$ , which has dimension 32 (including spin), is further split by electron–hole Coulomb and exchange interactions, as shown in Figure 1d.

In this work, we consider the excitonic manifold of nearly spherical, rock salt PbSe quantum dots. This material defines a new excitonic prototype, in that both the VBM states and the CBM states originate from the L valleys of the bulk fcc Brillouin zone. Because the L valley is 4-fold degenerate, the dimension of the excitonic manifold is 64 (including spin). However, quantum-confined electronic states derived from the bulk L valleys are split by intervalley coupling, interband coupling, effective mass anisotropy, and finite barrier confinement.<sup>12,13</sup> Electron–hole Coulomb and exchange interactions induce additional splittings of the excitonic energy levels. To clarify these effects, we have calculated the excitonic fine structure of PbSe quantum dots of radius  $R = 15.3 \text{ \AA}$  and  $R = 30.6 \text{ \AA}$  using a configuration–interaction approach.<sup>8,9</sup> We identify two main energy splittings, both of which are accessible to experimental probe: (i) The intervalley splitting  $\delta$  is the energy difference between the two near-edge peaks of the absorption spectrum. We find  $\delta = 80 \text{ meV}$  for the  $15.3 \text{ \AA}$  radius dot, and  $\delta = 18 \text{ meV}$  for the  $30.6 \text{ \AA}$  radius dot. (ii) The exchange splitting  $\Delta_x$  is the energy difference between the lowest-energy optically *dark* exciton state and the lowest-energy optically *bright* exciton state. We find that  $\Delta_x$  decreases from  $17 \text{ meV}$  for  $R =$

$15.3 \text{ \AA}$  to  $2 \text{ meV}$  for  $R = 30.6 \text{ \AA}$ . (iii) Interestingly, while in CdSe dots, the exciton splits into a lower-energy dark doublet and a higher-energy bright doublet, in PbSe dots the lowest-energy exciton state is a nondegenerate dark state, followed by a triply degenerate bright state. (iv) Our calculated exciton fine structure gives the temperature dependence of the radiative lifetime  $\tau_R$ . At room temperature,  $\tau_R$  is  $\sim 10^2\text{--}10^3 \text{ ns}$ , considerably longer than  $\sim 10 \text{ ns}$  in CdSe dots, in quantitative agreement with experiment.<sup>14,15</sup> We discuss our calculated results in view of recent experimental measurements of Stokes shift and radiative lifetime of PbSe colloidal quantum dots.

**Method of Calculation.** We use the following three steps to calculate the fine structure of low-energy exciton states.<sup>8,12,13,16</sup>

In step 1, we calculate the single-particle eigenstates of a quantum dot by solving the effective Schrödinger equation:

$$\left[-\frac{1}{2}\nabla^2 + V(\mathbf{r}) + \hat{V}_{\text{SO}}\right]\psi_i(\mathbf{r}, \sigma) = \epsilon_i \psi_i(\mathbf{r}, \sigma) \quad (1)$$

where the wave functions  $\psi_i(\mathbf{r}, \sigma)$  are expanded in a plane wave basis set. The spin–orbit coupling operator  $\hat{V}_{\text{SO}}$  is given by

$$\hat{V}_{\text{SO}} = \sum_{n,\alpha,l} \lambda_{\text{SO}} V_{l,\alpha}^{\text{SO}}(\mathbf{r} - \mathbf{R}_{n,\alpha}) |l\rangle_{\mathbf{R}_{n,\alpha}} \mathbf{L} \cdot \mathbf{S} \langle l|_{\mathbf{R}_{n,\alpha}} \quad (2)$$

where  $\langle l|_{\mathbf{R}_{n,\alpha}}$  is a projection operator of orbital angular momentum  $l$  centered at  $\mathbf{R}_{n,\alpha}$ , and  $V_{l,\alpha}^{\text{SO}}$  is a Gaussian  $p$ -like potential. The case  $\lambda_{\text{SO}} = 0$  corresponds to no spin–orbit, while  $\lambda_{\text{SO}} = 1$  corresponds to the full spin–orbit coupling regime. The local potential,  $V(\mathbf{r})$  is represented as a superposition of screened atomic pseudopotentials for atom species  $\alpha$  at site  $\mathbf{R}_{n,\alpha}$

$$V(\mathbf{r}) = \sum_{n,\alpha} v_\alpha(|\mathbf{r} - \mathbf{R}_{n,\alpha}|) \quad (3)$$

The atomic pseudopotentials  $v_\alpha(\mathbf{r})$  are fit to correct “LDA errors”, thus reproducing the bulk properties accurately.<sup>12</sup> Note that the potential  $V(\mathbf{r}) + V_{\text{SO}}$  allows for intervalley coupling, interband coupling, and spin–orbit coupling, as well as for realistic quantum confinement (due to the passivating atoms, not an infinite potential barrier). Thus, the single-particle wave functions  $\psi_i$  manifest all such effects, and are different from “model wave functions” used previously as a basis to calculate electron–hole exchange splittings.<sup>6</sup>

We consider here two PbSe dots of radius  $R = 15.3 \text{ \AA}$  and  $R = 30.6 \text{ \AA}$  ( $16.7 \text{ \AA}$  and  $31.9 \text{ \AA}$ , including passivation, respectively). The dots are constructed by placing a Se atom at the center of a sphere with an effective radius  $R$ , and then adding Pb and Se atoms within  $R$  according to the rocksalt lattice structure of bulk PbSe (lattice constant  $a_0 = 6.117 \text{ \AA}$ ). For such large dots, the electronic properties do not change much if we place a Pb atom at the dot center.

The effective radius  $R$  is calculated using the formula  $R = a_0(\gamma N_{\text{dot}})^{1/3}$ , where  $\gamma = 3/32\pi$  and  $N_{\text{dot}}$  is the total number of real atoms in the dot. The dangling bonds at the surface of the quantum dots are passivated by “ligand potentials”, in order to remove all surface states<sup>16</sup> from the dot band gap to  $\sim 1$  eV away from the band edges.

In step 2, we calculate electron–hole Coulomb ( $J$ ) and exchange ( $K$ ) integrals using the single-particle eigenfunctions  $\psi_i(\mathbf{r}, \sigma)$  of eq 1 as follows:

$$J_{v,c,v',c'} = \sum_{\sigma_1, \sigma_2} \int \int \frac{\psi_v^*(\mathbf{r}_1, \sigma_1) \psi_{c'}^*(\mathbf{r}_2, \sigma_2) \psi_v(\mathbf{r}_1, \sigma_1) \psi_c(\mathbf{r}_2, \sigma_2)}{\epsilon(\mathbf{r}_1, \mathbf{r}_2) |\mathbf{r}_1 - \mathbf{r}_2|} d\mathbf{r}_1 d\mathbf{r}_2$$

$$K_{v,c,v',c'} = \sum_{\sigma_1, \sigma_2} \int \int \frac{\psi_v^*(\mathbf{r}_1, \sigma_1) \psi_{c'}^*(\mathbf{r}_2, \sigma_2) \psi_{c'}(\mathbf{r}_1, \sigma_1) \psi_v(\mathbf{r}_2, \sigma_2)}{\epsilon(\mathbf{r}_1, \mathbf{r}_2) |\mathbf{r}_1 - \mathbf{r}_2|} d\mathbf{r}_1 d\mathbf{r}_2 \quad (4)$$

To evaluate the integrals, two different microscopic dielectric functions have been tested: (i) the modified Penn model<sup>8</sup> and (ii) the mask function model,

$$1/\epsilon(\mathbf{r}_1, \mathbf{r}_2) = 1/\epsilon_{\text{out}}(\mathbf{r}_1, \mathbf{r}_2) + [1/\epsilon_{\text{in}}(\mathbf{r}_1, \mathbf{r}_2) - 1/\epsilon_{\text{out}}(\mathbf{r}_1, \mathbf{r}_2)] m(\mathbf{r}_1) m(\mathbf{r}_2) \quad (5)$$

where  $m(\mathbf{r})$  is 1 for  $|\mathbf{r}| \leq R_{\text{eff}} - d$  ( $d = 1 \text{ \AA}$ ), decays smoothly to zero at  $|\mathbf{r}| = R_{\text{eff}} + d$  as  $\sqrt{[\sin(\pi(R_{\text{eff}} - |\mathbf{r}|)/2d) + 1]/2}$ , and remains zero for  $|\mathbf{r}| \geq R_{\text{eff}} + d$ . As recently shown by Cartoixa and Wang,<sup>17</sup> the dielectric function inside a quantum dot is bulk-like, whereas at the surface, it decays into the dielectric function of the material surrounding the quantum dot. Thus, a carrier can experience the screening of the surrounding material because there is a possibility that the charge distribution may spill out of the dot surface. We find that the optical absorption spectra calculated using the two types of dielectric functions (i) and (ii) are characteristically similar, and the topology of the absorption peaks remains unchanged. Hence, we shall use the dielectric function (ii) in all forthcoming calculations unless specified otherwise.

In step 3, we perform configuration interaction<sup>8</sup> (CI) calculations, where the exciton wave functions  $\Psi^{(\gamma)}$  are constructed as linear combinations of a set of single-substitution Slater determinants  $\Phi_{v,c}$  composed of the anti-symmetrized products of the single-particle wave functions  $\psi_i(\mathbf{r}, \sigma)$  of eq 1:

$$\Psi^{(\gamma)} = \sum_{v=1}^{N_v} \sum_{c=1}^{N_c} A_{v,c}^{(\gamma)} \Phi_{v,c} \quad (6)$$

Here  $N_c$  ( $N_v$ ) denotes the number of conduction (valence) states included in the expansion of the exciton wave functions. The coefficients  $A_{v,c}^{(\gamma)}$  are the eigenstates of the CI Hamiltonian in the basis set  $\{\Phi_{v,c}\}$ :

$$\sum_{v=1}^{N_v} \sum_{c=1}^{N_c} H_{v,c,v',c'} A_{v',c'}^{(\gamma)} = E_{\gamma} A_{v,c}^{(\gamma)} \quad (7)$$

The CI Hamiltonian is constructed using the Coulomb and exchange integrals of eq 4 as

$$H_{v,c,v',c'} \equiv \langle \Phi_{v,c} | H | \Phi_{v',c'} \rangle = (\epsilon_c - \epsilon_v) \delta_{v,v'} \delta_{c,c'} - J_{v,c,v',c'} + K_{v,c,v',c'} \quad (8)$$

Once the exciton wave functions have been obtained by diagonalizing the CI Hamiltonian, the dipole matrix elements relevant to interband optical transitions are calculated as follows:

$$\mathbf{M}_{\gamma} = \sum_{v,c} A_{v,c}^{(\gamma)} \langle \psi_v | \mathbf{r} | \psi_c \rangle \quad (9)$$

and the absorption cross section is calculated using Fermi's golden rule:

$$I(\omega) \propto \frac{1}{V} \sum_{\gamma} |\mathbf{M}_{\gamma}|^2 \delta(\hbar\omega - E_{\gamma}) \quad (10)$$

where  $V$  is the volume of the supercell encaging the quantum dot.

The radiative lifetime  $\tau_R(T)$  at temperature  $T$  is computed using time-dependent perturbation theory and the Boltzmann statistics<sup>18</sup>

$$\frac{1}{\tau_R(T)} = \frac{\sum_{\gamma} (1/\tau_{\gamma}) e^{-(E_{\gamma} - E_0)/K_B T}}{\sum_{\gamma} e^{-(E_{\gamma} - E_0)/K_B T}} \quad (11)$$

where

$$\frac{1}{\tau_{\gamma}} = \frac{4nF^2\alpha\omega_{\gamma}^3}{3c^2} |\mathbf{M}_{\gamma}|^2 \quad (12)$$

Here  $E_0$  is the ground-state exciton energy,  $n = \sqrt{\epsilon_{\text{out}}}$  is the refractive index of the medium surrounding the quantum dot,  $F = 3\epsilon_{\text{out}}/(\epsilon_{\text{dot}} + 2\epsilon_{\text{out}})$  is the screening factor ( $\epsilon_{\text{dot}}$  is the effective dielectric constant of the quantum dot),  $\alpha$  is the fine structure constant,  $\omega_{\gamma} = E_{\gamma}/\hbar$ , and  $c$  is the speed of light. It should be noted that the bulk PbSe band gap has a strong temperature dependence<sup>19</sup> [ $E_g(T) = 125 + (400 + 0.256T^2)^{1/2} \text{ meV}$ ] due to strong electron–phonon coupling.<sup>19</sup> However, our pseudopotential calculation is done for a static lattice, neglecting electron–phonon coupling. In fact, the pseudopotential is fitted<sup>12</sup> to the room-temperature bulk band gap (278 meV). Therefore, in eq 12, we assume that all the states used to compute  $\tau_R(T)$  are rigidly shifted without affecting the exponent  $E_{\gamma} - E_0$ .

### Exciton level splitting of 30.6 Å radius PbSe quantum dot

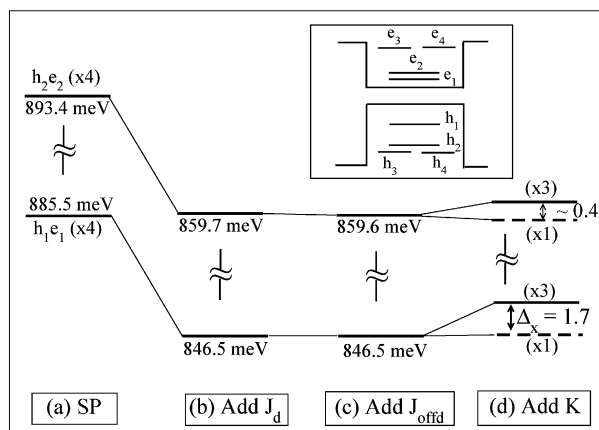


**Figure 2.** Calculated exciton levels of the 30.6 Å radius spherical PbSe quantum dot: (a) shows the single-particle (SP) results; (b) shows the results after adding the diagonal Coulomb energies ( $J_d$ ); (c) shows the effect of adding the off-diagonal Coulomb energies ( $J_{offd}$ ); (d) shows the results after adding the electron–hole exchange integrals (K). Optically allowed (forbidden) states are shown with solid (dashed) lines. The exchange splitting  $\Delta_x = 1.7$  meV is the splitting between the bright 3-fold degenerate level and the dark nondegenerate level (d). Intermediate excitonic levels that appear between the  $(h_1) \otimes (e_1)$  and the  $(h_2) \otimes (e_2)$  manifolds are orbitally forbidden, and are omitted for clarity, as are higher-energy levels. Inset: Band-edge single-particle energy levels.

**Excitonic Spectrum and its Deconvolution into Distinct Contributions: Excitonic Exchange-Splitting.** In PbSe quantum dots, the lowest-energy excitonic manifold originates from the electron–hole configurations  $(h_1 - h_4) \otimes (e_1 - e_4)$ . Since each single-particle state is doubly degenerate (because of Kramer’s degeneracy), the dimension of the full ground-state excitonic manifold is 64. These 64 excitonic states are split by intervalley and interband couplings as well as electron–hole Coulomb and exchange interactions. To identify the physical factors leading to the fine-structure splittings, we show in Figure 2 the evolution of the excitonic states originating from the configurations  $(h_1) \otimes (e_1)$  and  $(h_2) \otimes (e_2)$  as a function of the level of approximation used in the many-particle CI calculations. The configurations  $(h_1) \otimes (e_1)$  and  $(h_2) \otimes (e_2)$  are chosen because they have the largest oscillator strength. In the single-particle (SP) approximation (Figure 2a), we do not include electron–hole interactions, so the excitonic levels  $(h_1) \otimes (e_1)$  and  $(h_2) \otimes (e_2)$  are each 4-fold degenerate. Their energy separation (7.9 meV) is due to intervalley coupling. Figure 2b shows the effects of direct electron–hole Coulomb interaction. The  $(h_1) \otimes (e_1)$  level is lowered by 39 meV, while the  $(h_2) \otimes (e_2)$  level is lowered by 34 meV, but their 4-fold degeneracy remains intact. Off-diagonal Coulomb interactions (Figure 2c) are negligible and do not lift the degeneracy of the  $(h_1) \otimes (e_1)$  and  $(h_2) \otimes (e_2)$  levels. Finally, addition of electron–hole exchange interactions (Figure 2d) splits each 4-fold degenerate level into a lower-energy, nondegenerate dark level and a higher-energy, 3-fold degenerate bright level, separated by the exchange splitting  $\Delta_x$ .

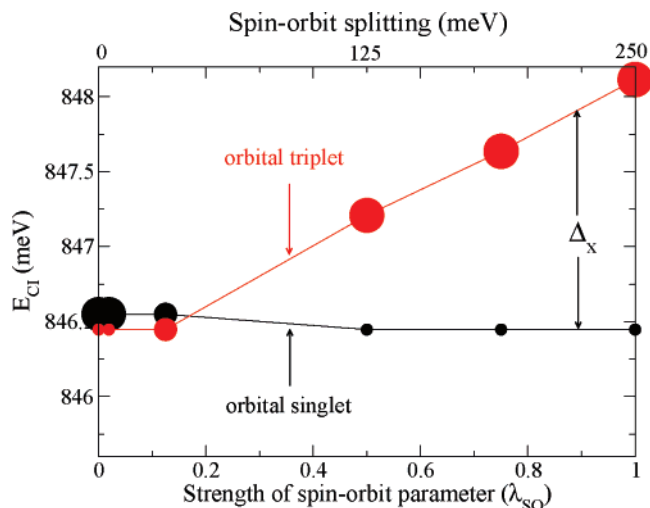


**Figure 3.** Evolution of the near-edge exciton states of a PbSe quantum dot ( $R = 30.6$  Å) as a function of the spin–orbit parameter  $\lambda_{SO}$  (see eq 2). The size of each filled dot represents the oscillator strength of the corresponding optical transition. In the low spin–orbit coupling regime ( $\lambda_{SO} = 0$ ), the optically forbidden triplet is below the optically allowed singlet. In the full spin–orbit coupling regime ( $\lambda_{SO} = 1$ ) the forbidden nondegenerate level is below the allowed 3-fold degenerate level.

**Effect of Spin–Orbit Interaction on Exchange Splitting.** Interestingly, the exchange splitting of the lowest excitonic level  $(h_1) \otimes (e_1)$  in PbSe quantum dots (Figure 1e) is qualitatively different from the exchange splittings of InP (Figure 1a), CdSe (Figure 1b), Si (Figure 1c), and Ge (Figure 1d) quantum dots, despite the fact that, in all these cases, the band-edge single-particle states ( $h_1$ ,  $h_2$ , and  $e_1$ ) have S-like envelope functions. (i) In zinc-blende InP dots with  $T_d$  point-group symmetry the  $(h_1, h_2) \otimes (e_1)$  8-fold degenerate exciton splits into a lower-energy, 5-fold degenerate dark level and a higher-energy, 3-fold degenerate bright level,<sup>7</sup> as shown in Figure 1a. (ii) In wurtzite CdSe dots, the  $(h_1) \otimes (e_1)$  exciton splits into a lower-energy, dark doublet and a higher-energy, bright doublet<sup>4,6,8,9</sup> (Figure 1b). (iii) In the case of Ge quantum dots (Figure 1d) the exchange splitting pattern is similar to that of InP, because the VBM ( $h_1 + h_2$ ) has the  $\Gamma_{8v}$  symmetry, while the CBM ( $e_1$ ) has the  $\Gamma_{6c}$  symmetry.<sup>11</sup> (iv) In PbSe dots, on the other hand, the  $(h_1) \otimes (e_1)$  exciton splits into a lower-energy, nondegenerate dark state and a higher-energy, 3-fold degenerate bright state, separated by the exchange splitting  $\Delta_x$ . This different behavior is due to the different character of the *bulk* Bloch functions from which the  $h_1$  and  $e_1$  states originate, which results in different spin–orbit coupling: In bulk InP and CdSe, the VBM and CBM are located at the  $\Gamma$  point of the Brillouin zone and have anion-p (VBM) and cation-s (CBM) orbital character. In bulk PbSe, on the other hand, both the VBM and the CBM are located at the L point of the Brillouin zone, and have mixed s and p orbital character. Figure 3 shows the evolution of the fine structure of the  $(h_1) \otimes (e_1)$  excitonic manifold as a function of the spin–orbit parameter  $\lambda_{SO}$  (see eq 2), for the  $R = 30.6$  Å quantum dot. In Figure 3, the spin–orbit parameter  $\lambda_{SO}$  is gradually turned on, and the excitonic manifold is recalculated for each value of  $\lambda_{SO}$ . For  $\lambda_{SO} = 0$



(no spin–orbit coupling), the  $(h_1) \otimes (e_1)$  exciton splits into a lower-energy spin triplet (dark) and a higher-energy spin singlet (bright). This type of exchange splitting was found for example in calculations of the excitonic fine structure of Si quantum dots,<sup>5,10</sup> where the spin–orbit coupling was neglected (see Figure 1c). As  $\lambda_{\text{SO}}$  is gradually increased (Figure 3), the lowest excitonic level becomes a nondegenerate dark state, while the higher excitonic level becomes a 3-fold degenerate bright state. This result indicates that spin–orbit coupling dramatically alters the excitonic fine structure of PbSe quantum dots and that the spin-singlet and spin-triplet characters are heavily intermixed in the presence of spin–orbit coupling. Because the orbital character of the band-edge single-particle wave functions is the same for other PbSe quantum dots in this size range, we expect that the fine-structure splitting shown in Figure 3 is a characteristic feature of PbSe quantum dots.

**Optical Absorption, Intervalley Splitting, and Stokes Shift.** Figure 4 shows the calculated near-edge optical absorption spectrum of the  $R = 15.3 \text{ \AA}$  and  $R = 30.6 \text{ \AA}$  PbSe quantum dots as a function of the level of CI approximation. Also shown in Figure 4 (vertical lines) are the 64 individual optical transitions that constitute the ground-state manifold. Green upward lines correspond to optically allowed transitions, while red downward lines denote optically forbidden transitions. We see from Figure 4 that the near-edge absorption spectrum consists of two main peaks, separated by  $\delta$ . This splitting  $\delta$  is present even in the SP approximation and is due primarily to intervalley splitting. The splitting between the lowest-energy dark state and the lowest-energy bright state, on the other hand, is due to electron–hole exchange interactions and corresponds to the exchange splitting  $\Delta_x$ . The intervalley splitting  $\delta$  and the exchange splitting  $\Delta_x$  are shown in Figure 5 for the two quantum dots considered here.

The Stokes shift (difference in energy between the emission peak and the first absorption peak) has been measured by several authors.<sup>14,20–22</sup> Wehrenberg et al.<sup>14</sup> reported a Stokes shift of  $\sim 22 \text{ meV}$  for PbSe quantum dots with emission peak at  $\sim 0.85 \text{ eV}$ , while Pietryga et al.<sup>20</sup> reported a Stokes shift of  $\sim 10 \text{ meV}$  for PbSe quantum dots with emission peak at  $0.49 \text{ eV}$ . Lifshitz et al.<sup>22</sup> recently measured the Stokes shift of PbSe quantum dots of different sizes. They reported Stokes shifts ranging from  $\sim 100 \text{ meV}$  for  $4 \text{ nm}$  diameter PbSe dots to  $-4 \text{ meV}$  (anti-Stokes shift) for  $6.3 \text{ nm}$  diameter PbSe dots.<sup>22</sup> These values span a much wider energy range than our calculated exchange splitting  $\Delta_x$  (see Figure 5). This could be due to the fact that the measured absorption peak is a convolution of the two band-edge absorption peaks (Figure 4), which are separated by the intervalley splitting  $\delta$ . These two peaks may be difficult to resolve experimentally, due to line broadening and size distribution effects. In addition, in very small PbSe quantum dots, ionic relaxation upon photoexcitation can lead to large Franck–Condon shifts,<sup>23,24</sup> which may also contribute to the experimentally observed Stokes shift. The origin of the observed anti-Stokes shift in large PbSe dots is presently unknown.<sup>22</sup> Our single-dot pseudopotential calculations show

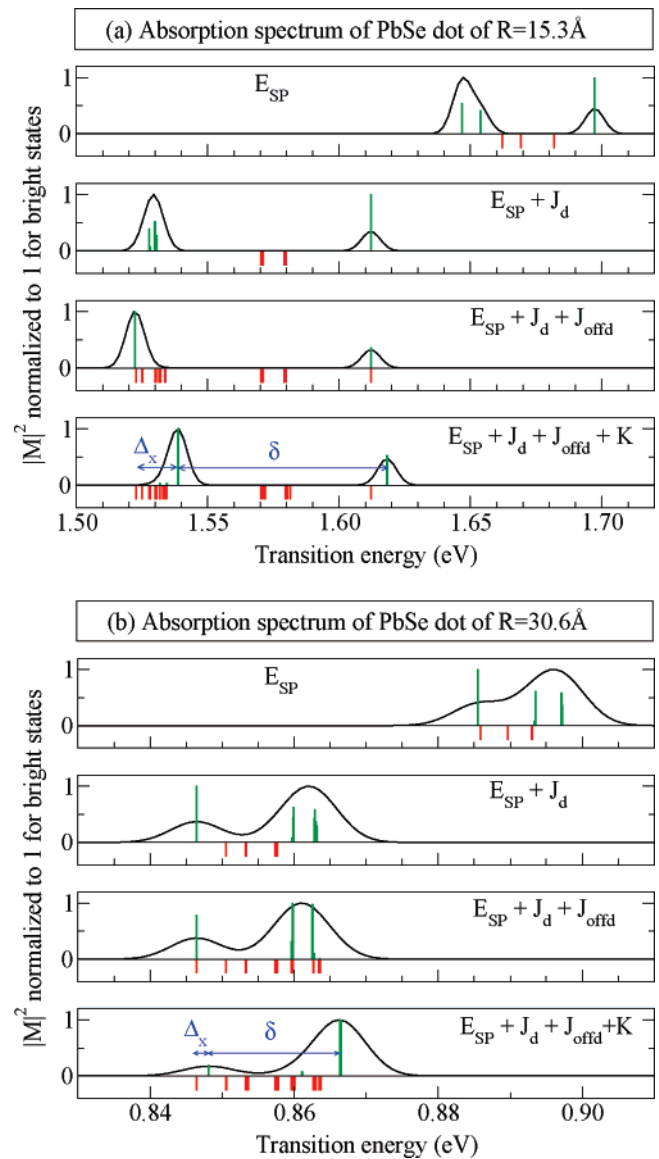


**Figure 4.** Optical absorption spectra (black solid lines) of (a)  $15.3 \text{ \AA}$  and (b)  $30.6 \text{ \AA}$  radius PbSe quantum dots calculated by progressively adding electron–hole Coulomb and exchange matrix elements (diagonal Coulomb, off-diagonal Coulomb, and electron–hole exchange interactions) to the CI Hamiltonian. The dipole matrix elements of optically allowed excitonic transitions are shown as green vertical bars on the positive scale, while forbidden transitions are shown as red vertical bars on the negative scale. The absorption spectrum is broadened by a Gaussian of width  $5 \text{ meV}$ . The exchange splitting  $\Delta_x$  and the intervalley splitting  $\delta$  are indicated by horizontal arrows in the lowest panel of each plot.

that the first absorption peak has higher energy than the emission peak in the dots considered here (Figure 4), which appears to rule out excitonic fine-structure splittings as the origin of the observed anti-Stokes shift.

Schaller et al.<sup>25</sup> examined the effective degeneracy of the main absorbing states in PbSe dots by fitting the bleaching curves to a model of size-dispersed dots with level degeneracy of either 2 or 8, finding good agreement for the assumed 8-fold degeneracy. This result does not conflict with the predicted splittings  $\Delta_x$  and  $\delta$  noted above because the exciton fine-structure splittings are washed out by size-

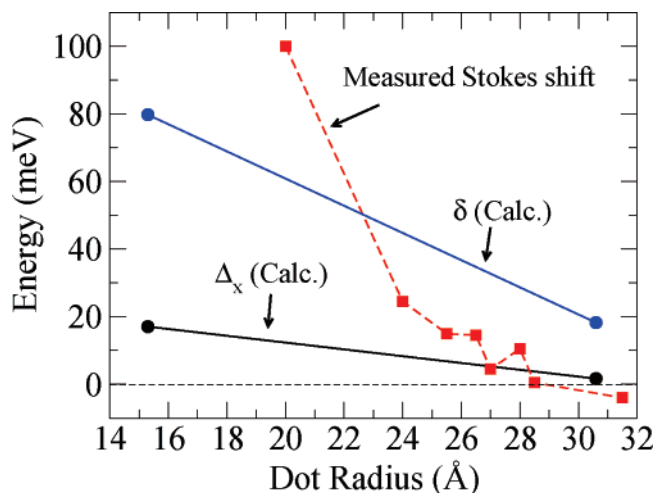


**Figure 5.** Calculated exchange splitting ( $\Delta_x$ ) and intervalley splitting ( $\delta$ ) as a function of dot radius, compared with the Stokes shift measured by Lifshitz et al.<sup>22</sup> The exchange splitting  $\Delta_x$  is defined as the energy difference between the first dark exciton level and the first bright exciton level. The intervalley splitting  $\delta$  is extracted from Figure 4, as defined therein at the CI level. The measured Stokes shift is the energy difference between the emission peak and the first absorption peak.

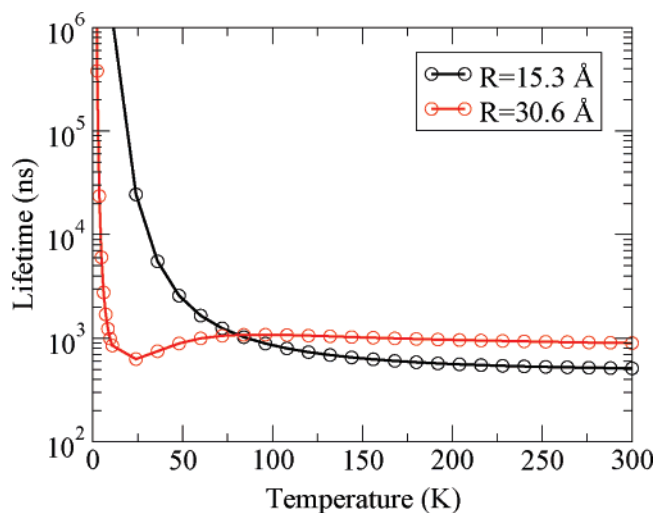


**Figure 6.** Calculated radiative lifetime  $\tau_R$  of PbSe quantum dots of radius  $R = 15.6$  and  $30.6$  Å as a function of temperature.

distribution effects and line-broadening in the procedure used by Schaller et al.<sup>25</sup>

**Radiative Lifetime.** Figure 6 shows the radiative lifetime  $\tau_R$  of PbSe quantum dots as a function of temperature  $T$ , calculated from eq 12. The effective dielectric constants  $\epsilon_{\text{dot}}$  of the dot is obtained using a modified Penn model<sup>8</sup> ( $\epsilon_{\text{dot}} = 10.77$  for  $R = 15.3$  Å, and  $\epsilon_{\text{dot}} = 15.69$  for  $R = 30.6$  Å). The dielectric constant of the surrounding matrix ( $\epsilon_{\text{out}} = 2.1$ , corresponding to chloroform) is chosen to be consistent with the experimental setup of Wehrenberg et al.<sup>14</sup> The computed room-temperature radiative lifetimes of PbSe dots of radius  $R = 15.3$  and  $30.6$  Å are 511 and 897 ns, respectively. The calculated value for the  $R = 30.6$  Å dot agrees very well with the measured<sup>14</sup> room-temperature lifetime of 880 ns for  $R = 29$  Å quantum dots. Du et al.<sup>15</sup> also reported measured radiative lifetimes of 200–500 ns at room temperature for

PbSe dots 15–30 Å in radius, which agrees with our results. It is interesting to note that the calculated lifetime increases with increasing dot size, which was also observed in experiment.<sup>15</sup>

The room-temperature radiative lifetime of PbSe dots<sup>14,15</sup> is much shorter than the radiative lifetime of Si quantum dots<sup>5</sup> (tens of  $\mu\text{s}$ ). The long lifetime of Si quantum dots can be explained by the indirect character of the Si bulk band gap. On the other hand, the room-temperature radiative lifetime of PbSe dots is considerably longer than the  $\sim 10$  ns radiative lifetime of CdSe dots<sup>18,26</sup> despite the fact that both materials have a direct band gap. To clarify the origin of this difference, we have chosen two PbSe and CdSe dots of similar size (15.3 and 14.0 Å in radius, respectively) and compared the oscillator strengths of the lowest-energy bright exciton states. The calculated oscillator strength of the bright state of the PbSe dot is smaller by a factor of 0.3 than that of the CdSe dot. This is caused by the intervalley coupling among the four equivalent L points in the Brillouin zone that mixes the phases of the Bloch part of dot wave functions, so that the oscillator strength in PbSe dots becomes smaller compared to that of CdSe dots. We conclude that the long radiative lifetime of PbSe quantum dots is determined primarily by the orbital character of the band-edge single-particle wave functions and not by the magnitude of the electron–hole exchange splitting.

In summary, we identify two main energy splittings in the exciton fine structure of PbSe colloidal quantum dots: (i) The intervalley splitting  $\delta$  is the energy difference between the two near-edge absorption peaks. We find  $\delta = 80$  meV for  $R = 15.3$  Å, and  $\delta = 18$  meV for  $R = 30.6$  Å. (ii) The exchange splitting  $\Delta_x$  is the energy difference between the lowest-energy optically dark exciton state and the first optically bright exciton state. We find that  $\Delta_x$  ranges between 17 meV for  $R = 15.3$  Å and 2 meV for  $R = 30.6$  Å. (iii) We also find that, while in CdSe dots having  $\Gamma$ -like VBM and CBM states the lowest exciton is a dark doublet, followed by a higher-energy bright doublet, in PbSe dots, the lowest state is a nondegenerate dark exciton, followed by a higher-energy 3-fold degenerate bright exciton. (iv) The calculated radiative lifetime at room temperature is  $\sim 100$  ns, considerably longer than  $\sim 10$  ns in CdSe dots, in quantitative agreement with experiment. The measured Stokes shift by Lifshitz et al.<sup>22</sup> span a much wider energy range than our calculated exchange splitting, suggesting that the measured Stokes shift might be due primarily to the large intervalley splittings of the single-particle transitions.

**Acknowledgment.** We thank F. Wise for illuminating discussions and E. Lifshitz for allowing us to use her data in ref 22. This work was funded by the U.S. Department of Energy, Office of Science, Basic Energy Science, Materials Sciences and Engineering, under contract no. DE-AC36-99GO10337 to NREL.

## References

- (1) Takagahara, T. *Phys. Rev. B* **1993**, *47*, 4569.
- (2) Banin, U.; Lee, C. J.; Guzelian, A. A.; Kadavanich, A. V.; Alivisatos, A. P.; Jaskolski, W.; Bryant, G. W.; Efros, A. L.; Rosen, M. *J. Chem.*

- Phys.* **1998**, *109*, 2306; Banin, U.; Lee, C. J.; Guzelian, A. A.; Kadavanich, A. V.; Alivisatos, A. P. *Superlattices Microstruct.* **1997**, *22*, 559.
- (3) Chamarro, M.; Dib, M.; Voliotis, V.; Filoramo, A.; Roussignol, P.; Gacoin, T.; Boilot, J. P.; Delerue, C.; Allan, G.; Lannoo, M. *Phys. Rev. B* **1998**, *57*, 3729.
  - (4) Chamarro, M.; Gourdou, C.; Lavallard, P. *Phys. Rev. B* **1996**, *53*, 1336.
  - (5) Calcott, P. D. J.; Nash, K. J.; Canham, L. T.; Kane, M. J.; Brumhead, D. *J. Phys.: Condens. Matter* **1993**, *5*, L91.
  - (6) Efros, A. L.; Rosen, M.; Kuno, M.; Nirmal, M.; Norris, D. J.; Bawendi, M. *Phys. Rev. B* **1996**, *54*, 4843; Nirmal, M.; Norris, D. J.; Kuno, M.; Bawendi, M. G. *Phys. Rev. Lett.* **1995**, *75*, 3728; Norris, D. J.; Efros, A. L.; Rosen, M.; Bawendi, M. G. *Phys. Rev. B* **1996**, *53*, 16347.
  - (7) Micic, O. I.; Cheong, H. M.; Fu, H.; Zunger, A.; Sprague, J. R.; Mascarenhas, A.; Nozik, A. J. *J. Phys. Chem. B* **1997**, *101*, 4904; Fu, H.; Zunger, A. *Phys. Rev. B* **1997**, *56*, 1496.
  - (8) Franceschetti, A.; Fu, H.; Wang, L. W.; Zunger, A. *Phys. Rev. B* **1999**, *60*, 1819.
  - (9) Franceschetti, A.; Wang, L. W.; Fu, H.; Zunger, A. *Phys. Rev. B* **1998**, *58*, R13367.
  - (10) Reboredo, F. A.; Franceschetti, A.; Zunger, A. *Phys. Rev. B* **2000**, *61*, 13073.
  - (11) Reboredo, F. A.; Zunger, A. *Phys. Rev. B* **2001**, *63*, 235314.
  - (12) An, J. M.; Franceschetti, A.; Dudiy, S. V.; Zunger, A. *Nano Lett.* **2006**, *6*, 2728.
  - (13) Franceschetti, A.; An, J. M.; Zunger, A. *Nano Lett.* **2006**, *6*, 2191.
  - (14) Wehrenberg, B. L.; Wang, C.; Guyot-Sionnest, P. *J. Phys. Chem. B* **2002**, *106*, 10634.
  - (15) Du, H.; Chen, C.; Krishnan, R.; Krauss, T. D.; Harbold, J. M.; Wise, F. W.; Thomas, M. G.; Silcox, J. *Nano Lett.* **2002**, *2*, 1321.
  - (16) Wang, W.; Zunger, A. *Phys. Rev. B* **1995**, *51*, 17398; Canning, A.; Wang, L. W.; Williamson, A.; Zunger, A. *J. Comput. Phys.* **2000**, *160*, 29.
  - (17) Cartoixa, X.; Wang, L.-W. *Phys. Rev. Lett.* **2005**, *94*, 236804.
  - (18) Califano, M.; Franceschetti, A.; Zunger, A. *Nano Lett.* **2005**, *5*, 2360.
  - (19) Landolt and Börtstein, Group III Condensed Matter; Springer-Verlag: Berlin, 1998; Vol 41.
  - (20) Pietryga, J. M.; Schaller, R. D.; Werder, D.; Stewart, M. H.; Klimov, V. I.; Hollingsworth, J. A. *J. Am. Chem. Soc.* **2004**, *126*, 11752.
  - (21) Harbold, J. M.; Du, H.; Krauss, T. D.; Cho, K. S.; Murray, C. B.; Wise, F. W. *Phys. Rev. B* **2005**, *72*, 195312.
  - (22) Lifshitz, E.; Brumer, M.; Kigel, A.; Sashchiuk, A.; Bashouti, M.; Sirota, M.; Galun, E.; Burshtein, Z.; Le Quang, A. Q.; Ledoux-Rak, I.; Zyss, J. *J. Phys. Chem. B* **2006**, *110*, 25356.
  - (23) Franceschetti, A.; Pantelides, S. T. *Phys. Rev. B* **2003**, *68*, 033313.
  - (24) Puzder, A.; Williamson, A. J.; Grossman, J. C.; Galli, G. *J. Am. Chem. Soc.* **2003**, *125*, 2786.
  - (25) Schaller, R. D.; Petruska, M. A.; Klimov, V. I. *J. Phys. Chem. B* **2003**, *107*, 13765.
  - (26) Crooker, S. A.; Barrick, T.; Klimov, V. I. *Appl. Phys. Lett.* **2003**, *82*, 2793.

NL071219F